Tuning Ionic Conductivity and Structural Stability of $LiHf_2(PO4)_3$ Solid Electrolytes through Al Substitution

Pratiksha Gami and Sunil Kumar*

Department of Metallurgical Engineering and Materials Science, Indian Institute of Technology Indore, Simrol, 453552, India.

*Corresponding author, E-mail: sunil@iiti.ac.in

Keywords: Solid-state batteries, NASICON, Ionic conductivity, and GCD.

Abstract

Rechargeable Li-metal batteries with solid electrolytes offer enhanced safety and higher specific capacity than conventional liquid-electrolyte-based Li-ion batteries. However, low Li-ion conductivity and high interfacial resistance between the electrolyte and electrode often hinder their performance. In this study Al-substituted $LiHf_2(PO_4)_3$ inorganic electrolytes are fabricated *via* the conventional solid-state reaction method. The Rietveld refinement of room temperature X-ray diffraction (XRD) data confirms a rhombohedral phase. The highest total ionic conductivity was observed for 25% Al substitution at the Hf site (7.09×10^{-5} S cm^{-1}). The activation energy for total ionic conductivity decreased from 0.50 eV to 0.29 eV with increasing aluminum substitution till $x = 0.5$. The Li-ion transference number was ~ 0.99, indicating that lithium-ion dominates the charge transport in the material. Electrochemical stability tests using linear sweep voltammetry revealed the ceramic electrolyte's stability up to approximately 4.61 V. The $Li_{1.5}Al_{0.5}Hf_{1.5}(PO_4)_3$ electrolyte demonstrated a stable lithium plating/stripping in a Li||Li cell for over 170 h. Furthermore, when employed in a solid-state Li||$LiFePO_4$ cell, it exhibited high Coulombic efficiency and decent cycling stability, demonstrating its potential for use in high-temperature solid-state batteries.

Introduction

The increasing demand for consumer electronics and electric vehicles has intensified efforts to develop high-energy-density rechargeable batteries, with Li-based technologies demonstrating superior performance [1-5]. Solid-state electrolytes offer distinct advantages over their liquid counterparts, notably the prevention of electrode corrosion and enhanced battery safety [6-9]. All-solid-state batteries utilizing alkali-metal anodes have attracted considerable attention due to the low reduction potential (-3.04 V *vs.* SHE) and high specific capacity (~3680 mAh g^{-1}), which significantly increases the energy density of the system [10-13]. For optimal performance, solid electrolytes must exhibit high room temperature (RT) lithium-ion conductivity, minimal interfacial resistance with various cathode/anode, excellent stability in ambient conditions, and a wide electrochemical window [14-18]. The development of novel solid electrolytes that meet all these criteria remains a considerable scientific and engineering challenge [19-23]. Accordingly, various classes of solid-state electrolytes are being extensively studied, including organic electrolytes and ceramic electrolytes based on sulfides, halides, and oxides [20, 24-29]. Flexible organic electrolytes are easily prepared and exhibit low interfacial resistance with lithium metal anodes [20, 30]. However, they typically exhibit low lithium-ion conductivity (~ 1×10^{-6} S cm^{-1} at RT) due to the slow segmental motion of the polymer chains. Additionally, their low lithium-ion transference number (<0.5) leads to concentration polarization in all-solid-state batteries [31, 32]. Sulfide-based electrolytes offer higher lithium-ion conductivity (~ 1×10^{-3} S cm^{-1}), but they are highly sensitive to moisture and exhibit narrow electrochemical windows [33, 34]. On the other hand, oxide-based lithium-ion conductors are more susceptible to ambient conditions, and some, such as the garnet electrolyte $Li_7La_3Zr_2O_{12}$, demonstrate excellent properties with a wide electrochemical window (>5 V), high lithium-ion conductivity (1×10^{-3} S cm^{-1}) [35]. Nevertheless, the fast lithium-ion/proton exchange in

garnets under ambient conditions leads to the formation of a Li_2CO_3 insulating layer on the surface, increasing interfacial resistance with the lithium metal anode [36-38].

NASICON-type electrolytes, like $Li_{1.5}Al_{0.5}Ti_{1.5}(PO_4)_3$ and $Li_{1.5}Al_{0.5}Ge_{1.5}(PO_4)_3$, have been widely used due to their high lithium-ion conductivity and robust stability in moist air, attributed to the strong covalent P^{5+} - O^{2-} bonds [39-42]. However, the instability of Ti^{4+}/Ge^{4+} ions with lithium metal still limits their practical application [43, 44]. Replacing Ti^{4+}/Ge^{4+} with more stable metal ions could enhance their compatibility with lithium metal [45-47]. This work explores the potential of Hf-based NASICON electrolytes, which offer a promising alternative for improving stability and performance in solid-state lithium batteries.

Lithium hafnium phosphate ($LiHf_2(PO_4)_3$, LHP) crystallizes in a NASICON-type structure, but it faces challenges due to a topotactic and reversible phase transition at low temperatures [48, 49]. Research on LHP has been sparse, primarily due to difficulties related to its poor sintering behavior and the contentious phase transition that occurs during its synthesis process [50-52]. To date, the substitution of aluminum (Al) into LHP has only been reported by Chang et al. and Zangina et al., focusing on the synthesis and electrical properties of prepared ceramic samples [53, 54]. In this work, we synthesized and characterized a series of $Li_{1+x}Al_xHf_{2-x}(PO_4)_3$ (x = 0, 0.2, 0.4, 0.5, and 0.6) samples, employing X-ray diffraction (XRD), scanning electron microscopy (SEM), and electrochemical impedance spectroscopy (EIS). The findings show that Al^{3+} doping enhances the conductivity of the doped samples compared to the pure $LiHf_2(PO_4)_3$. Specifically, $Li_{1.5}Al_{0.5}Hf_{1.5}(PO_4)_3$ (referred to as 0.5Al-LHP) exhibited the highest RT lithium-ion conductivity of 7.09×10^{-5} S cm^{-1}. Additionally, symmetric Li||Li cells and solid-state Li||LiFePO4 cells were fabricated, with the results substantiating the promising electrochemical performance of the 0.5Al-LHP pellet.

Materials and Methods

Synthesis of ceramic solid electrolyte $Li_{1+x}Al_xHf_{2-x}(PO_4)_3$

The polycrystalline $Li_{1+x}Al_xHf_{2-x}(PO_4)_3$ compounds with values of x = 0, 0.2, 0.4, 0.5, and 0.6 (denoted as xAl-LHP) were synthesized through a solid-state reaction method. The starting materials included corresponding stoichiometric quantities of Li_2CO_3, HfO_2, Al_2O_3, and $NH_4H_2PO_4$. These components were thoroughly mixed using a mortar and pestle, then heated in an alumina crucible at 500 °C, followed by 800 °C for 12 h. After this, the mixture was ground again, and the resulting powders were compressed into pellets with a 10 mm diameter. Green ceramic pellets were heated at varying temperatures to ascertain the optimal sintering and calcination conditions (900 - 1000 °C). Sacrificial powder of the same composition was employed to bury the pellets, mitigating lithium volatilization during sintering at temperatures above 950 °C.

Synthesis of Cathode

The cathodes comprised $LiFeO_4$, super P, and polyvinylidene fluoride (PVDF) in an 8:1:1 mass ratio. The powders were mixed using N-methylpyrrolidone in a beaker. A uniform film was coated onto Al foil using the automatic slurry coater machine and dried at 60 °C for 6 h. The dried electrodes were converted into 6 mm discs, yielding a mass loading of ~1.3 mg cm^{-2}.

Characterization techniques

The crystallographic structure of the xAl-LHP powders was characterized using X-ray diffraction (XRD) measurements, performed on an Empyrean - Malvern Panalytical instrument with Cu Kα radiation over a 2θ range of 10° - 60°. Rietveld refinements of the XRD data were carried out using TOPAS academic software to determine the crystallographic parameters [55]. The morphology and microstructure of the pellets, along with the distribution of elements, were analyzed using scanning

electron microscopy (SEM, JSM7500F) coupled with energy dispersive spectrometry (EDS). Polished samples were utilized for ionic conductivity measurements. Silver electrodes were applied on either side of pellets to act as the Li-ion blocking electrode for electrochemical impedance spectroscopy (EIS) measurements, which were conducted using a Biologic instrument across a frequency range of 100 Hz to 10 MHz. Before EIS measurements, the samples were vacuum-dried at 100 °C to eliminate moisture. Impedance data were analyzed and fitted using EIS analyzer software to calculate conductivity [56]. The total conductivity (σ) was determined using the formula $\sigma = l/aR$, where l is the sample thickness, a is the area, and R is the resistance obtained from the complex impedance plots. The activation energy (E_a) for ionic conductivity was derived from the Arrhenius equation ($\sigma = \sigma_0 \exp(-E_a/kT)$), where σ_0 is the pre-exponential factor, k is the Boltzmann constant, and T is the temperature. The t_{Li^+} was quantified through direct current (DC) polarization measurements, with an external voltage of 0.5 V applied to achieve a steady current. The critical current density (CCD) was ascertained by probing various current densities at RT to evaluate the maximum voltage tolerance with lithium metal. Linear sweep voltammetry (LSV) measurements for Li||SS cells were conducted to establish the stable voltage window for the sample. Symmetric (Li||Li) and full cells (Li||$LiFePO_4$) with liquid electrolyte on the cathode side, employing the 0.5Al-LHP pellet as the solid electrolyte, were tested in CR2032 coin cells using a Neware multichannel battery testing system. X-ray photoelectron spectroscopy (XPS) was carried out using a Thermo Fisher Scientific Naxsa system equipped with a monochromatic Al Kα X-ray source (E = 1486.6 eV).

Result and discussion

X-ray diffraction (XRD) analysis was utilized to examine the phase composition of the synthesized ceramics. As shown in Figures S1-S5, the rhombohedral phase forms at 900 °C for the 0.2Al-LHP

composition and 950 °C for the 0.4Al-LHP composition. For the 0.5Al-LHP and 0.6Al-LHP samples, the rhombohedral phase appears at 1000 °C. Rietveld refinement of the rhombohedral phases across varying Al concentrations in $Li_{1+x}Al_xHf_{2-x}(PO_4)_3$ confirmed the $R\bar{3}c$ space group (Figure 1). In the refinement plots, open black circles, red solid lines, and grey bottom lines represent the observed, calculated, and difference profiles, respectively. The blue vertical bars at the bottom indicate the Bragg positions of the reflections. Additionally, a low-intensity peak belonging to the triclinic phase is observed at 20° (pink hash marks). An impurity phase, identified as $AlPO_4$ (green asterisks), is also observed [48, 57]. In the non-stoichiometric $Li_{1+x}Al_xHf_{2-x}(PO_4)_3$ structure, the excess lithium resides at the partially populated II site (Wyckoff site 18*e*), while Al and Hf are randomly distributed at the 12*c* site (Figure S6). The lithium occupancies were not refined due to their low electron density.

Figure 1

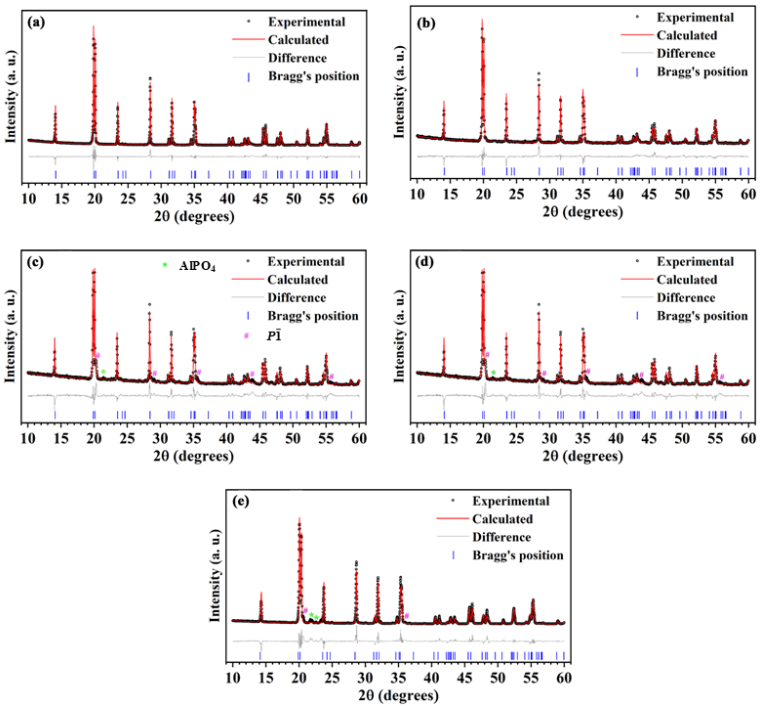

Figure 1. Rietveld refinement of powder XRD patterns for xAl-LHP with x = (a) 0, (b) 0.2, (c) 0.4, (d) 0.5, and (e) 0.6. The black open circles represent the observed data, the red solid line denotes the refinement result, and the blue vertical bars indicate the Bragg positions of the reflections.

The observed trends in the refined lattice parameters and unit cell volume of *x*Al-LHP are shown in Figure 2. Up to 0.5Al doping, the smaller Al^{3+} (0.535 Å) ions replace the larger Hf^{4+} (0.71 Å) ions, leading to a continuous decrease in the lattice parameters (*a* & *c)*, resulting in an overall decrease in the unit cell volume (*V*). However, the saturation of Al^{3+} in the structure implies a solubility limit of approximately $x \approx 0.5$, beyond which elevated Al^{3+} concentrations induce a pronounced decline in the *x*Al-LHP phase fraction [58]. The emergence of a secondary $AlPO_4$ phase is detected, and this structural reconfiguration induces an expansion of the '*c*' parameter, thereby increasing the unit cell volume [59]. To elucidate the expansion of the unit cell, Figures 2(d)-(e) depict the correlation between the volumes of the LiO_6 and MO_6 octahedra, along with the PO_4 tetrahedra, as a function of the nominal lithium content. The observed increase in the *c*-axis and unit cell volume appears to correspond closely with the enlargement of the LiO_6 octahedral volumes, as these structures are oriented along the *z*-direction (see Figure S6). The Li(6*a*) site shares a face with the $(Hf/Al)O_6$ octahedra along the *z*-direction, promoting lithium movement along the *c*-axis due to weaker Coulombic repulsion in this direction. While this factor alone does not account for the volume increase observed in the 0.6Al system, the enhanced occupancy of the adjacent Li(36*f*) sites, which amplifies Coulombic repulsion, likely contributes to the observed expansion of the LiO_6 polyhedra. This behavior can be attributed to a structural adjustment that minimizes Coulombic repulsion within the system [58, 60, 61]. All these verify the proposed hypothesis

that substituting Hf^{4+} for Al^{3+} may generate a similar influence to substituting Al^{3+} for $Zr^{4+}/Ti^{4+}/Ge^{4+}$, which stabilizes the rhombohedral phase at RT [58, 62, 63].

Figure 2

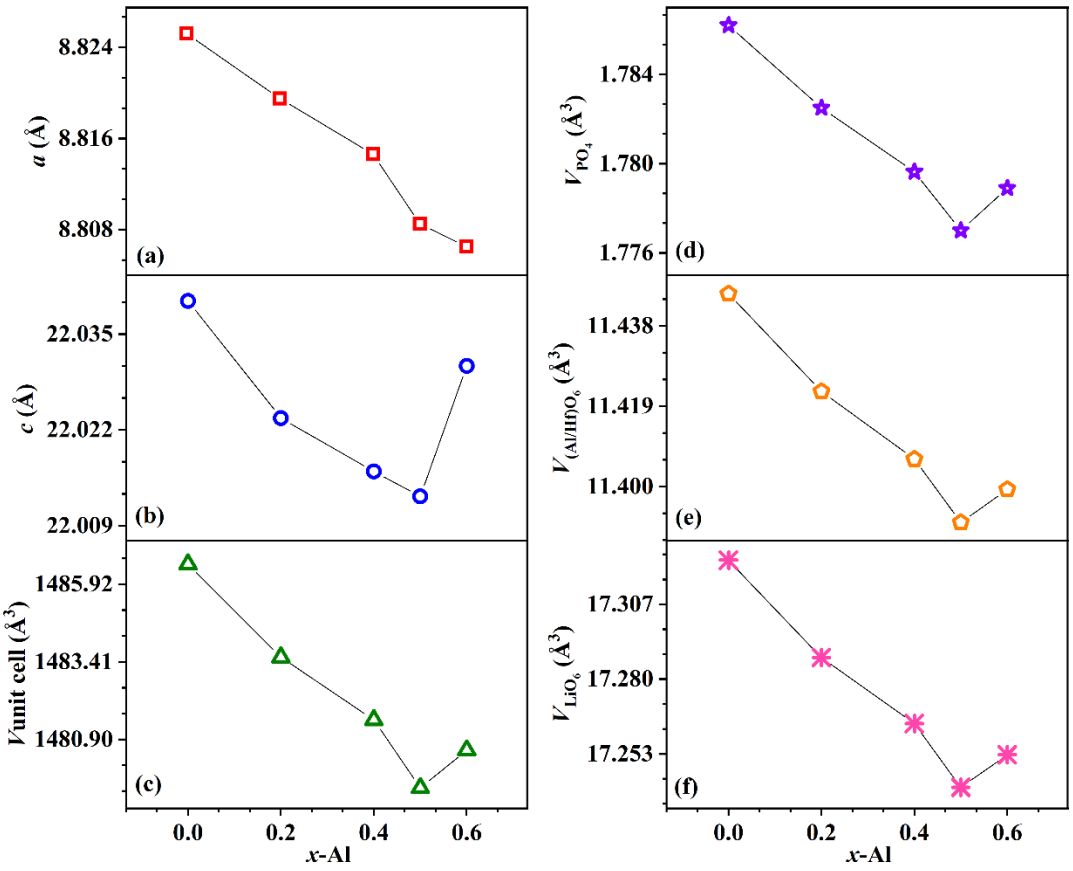

Figure 2. Variation of lattice parameters and unit cell volumes as a function of aluminum content (xAl): (a) Lattice parameter a, (b) lattice parameter c, (c) unit cell volume (V), (d) volume of PO_4, (e) volume of Al/HfO_6, and (f) volume of LiO_6.

Figure 3 presents the scanning electron microscopy (SEM) images of sintered pellets of $Li_{1+x}Al_xHf_{2-x}(PO_4)_3$ for various values of x, corresponding to the $R\bar{3}c$ phase. For the $LiHf_2(PO_4)_3$ pellet ($x = 0$), sintered at 1000 °C for 10 h, grains of varying sizes are observed, with noticeable inter-grain porosity. The relative density of this pellet is approximately 72%. In contrast, with the

introduction of Al^{3+} doping, a noticeable reduction in inter-grain pores is observed, leading to a significant improvement in the relative density up to x = 0.5 (Table S1). For the x = 0.6 composition, the grains are considerably larger. To assess the distribution of elements within the grains and grain boundaries, energy dispersive spectroscopy (EDS) was performed. The EDS results, presented in Figure S7, show that both Hf and Al are evenly distributed throughout the sample.

Figure 3

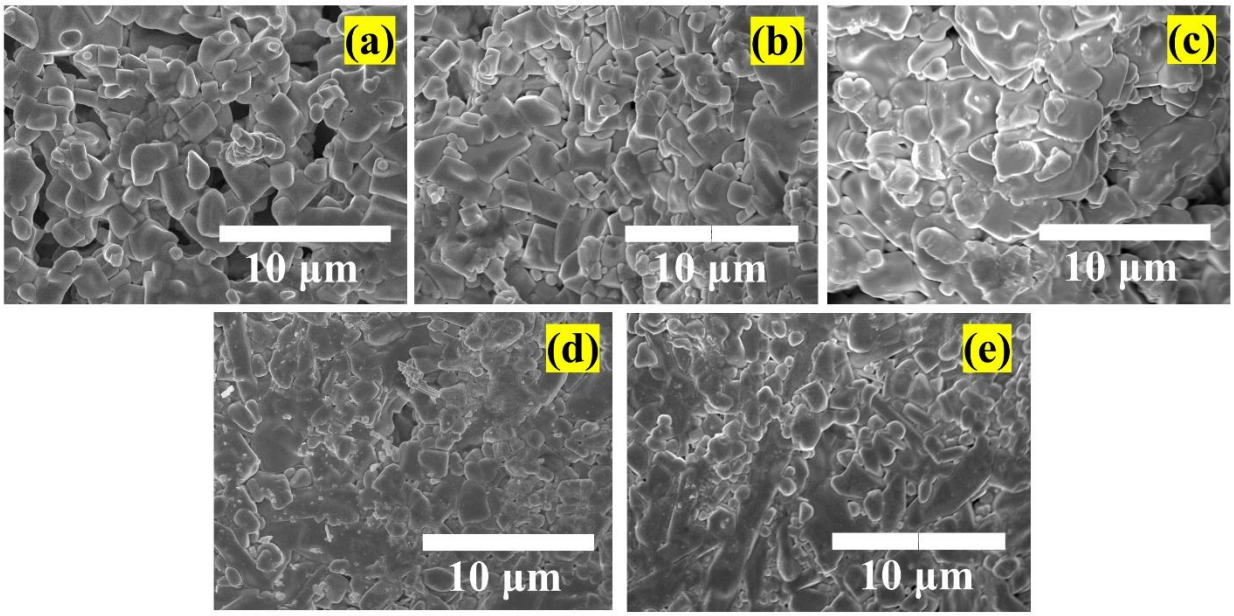

Figure 3. SEM micrographs of rhombohedral (a) 0Al-LHP, (b) 0.2Al-LHP, (c) 0.4Al-LHP, (d) 0.5Al-LHP, and (e) 0.6Al-LHP pellets.

Temperature-dependent impedance spectroscopy was conducted to investigate the influence of Al substitution on the ionic conductivity, with the impedance data presented in Figure 4. For compositions with x < 0.5, the Nyquist plots exhibit two distinct semicircles corresponding to grain and grain boundary resistances (Fig. 4(a-c)). At lower frequencies, a tail is observed, which can be attributed to the ion-blocking behavior of the silver electrodes. To model the impedance response,

an equivalent circuit consisting of $(R_g||Q_g)+(R_{gb}||Q_{gb})+Q_{el}$ was used, where subscripts g and gb indicate the grain and grain boundary contribution, respectively, and R & Q represents the resistance & constant phase element. Q_{el} accounts for the constant phase element of the blocking electrodes. For compositions $x = 0.5$ and 0.6, only a single depressed semicircle is observed at high frequency (representing the bulk and grain boundary responses), accompanied by a long tail at lower frequencies. In this case, it is challenging to deconvolute the contributions from the grain and grain boundary components separately. Therefore, the equivalent circuit $(R_t||Q_t)+Q_{el}$, where t represents the total (grains and grain boundaries) contribution, was used to fit the impedance data. Figure S8 displays a Bode plot of the impedance data, illustrating the consistency with the proposed equivalent circuit and confirming the quality of the fit, which suggests the presence of two distinct dielectric relaxations in the low- and high-frequency regions for samples with x up to 0.4. The total ionic conductivity reaches a maximum value of ~ 7.09×10^{-5} S cm^{-1} for $x = 0.5$. The enhanced ionic conductivity observed in the Al-substituted samples is thought to result from an increase in lithium content and a modification of the structural framework that facilitates Li-ion migration [58, 64, 65]. The reduction in grain boundary conductivity with Al substitution can be attributed to the enhanced densification of the material. However, when the Al doping level exceeds 0.5, the total conductivity decreases to 2.18×10^{-5} S cm^{-1} due to the increase in the fraction of impurity phases ($AlPO_4$), which negatively affects the ionic transport [61]. Previously, Zangina et al. reported the highest AC conductivity of approximately 2.5×10^{-5} S cm^{-1} in the $Li_{1+x}Al_xHf_{2-x}(PO_4)_3$ composition at $x = 0.25$ [53]. Additionally, Chang et al. demonstrated that Li^+ conductivity increases proportionally with sample density, with the highest recorded value of 1.1×10^{-4} S cm^{-1} observed in the spark plasma sintered $Li_{1.5}Al_{0.5}Hf_{1.5}(PO_4)_3$ [54].

Figure 4

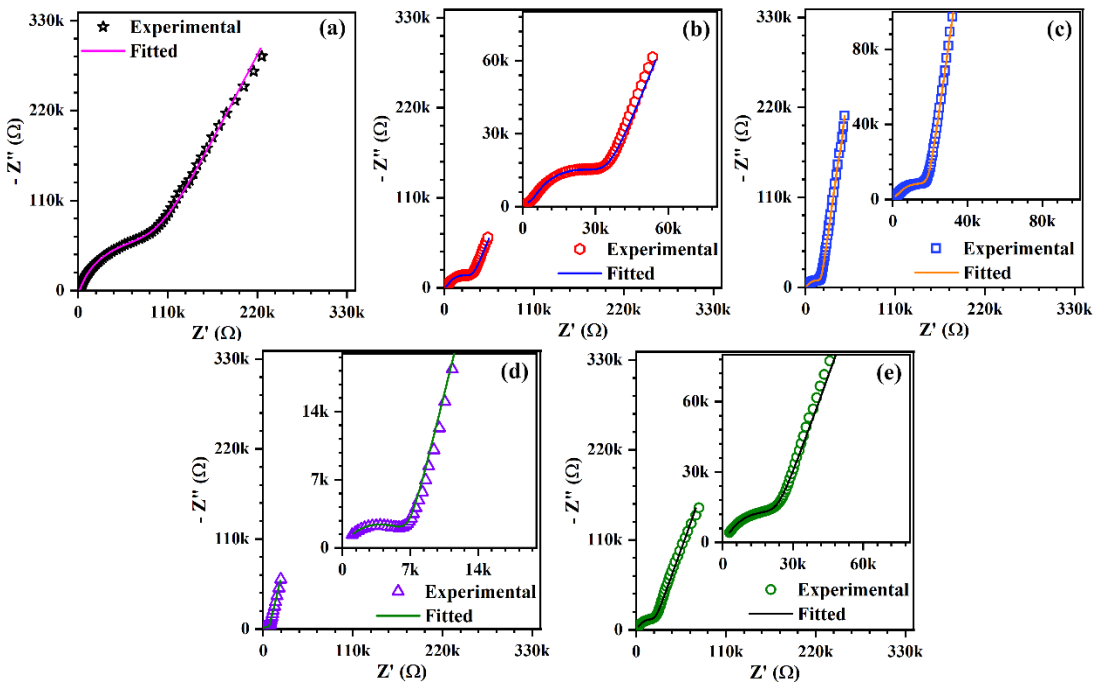

Figure 4. Nyquist plots of (a) 0Al-LHP, (b) 0.2Al-LHP, (c) 0.4Al-LHP, (d) 0.5Al-LHP, and (e) 0.6Al-LHP pellet at room temperature. The solid lines represent the fitted results. The (a-c) were fitted using the equivalent circuit model $(R_g||Q_g)+(R_{gb}||Q_{gb})+Q_{el}$*, while (d-e) were fitted using the circuit model* $(Rt||Qt)+Q_{el}$.

Figure 5a illustrates the temperature-dependent total ionic conductivity of rhombohedral $Li_{1+x}Al_xHf_{2-x}(PO_4)_3$. A clear linear relationship between $\log(\sigma_t)$ and 1000/T is observed for all Al-doped compositions, which aligns well with the Arrhenius equation. The activation energy (E_a) is determined from the slope of the fitted straight line. The E_a decreases progressively with increasing x, ranging from 0.50 eV at $x = 0$ to 0.29 eV at $x = 0.5$, followed by a further increase for $x = 0.6$ (0.34 eV), following a trend similar to ionic conductivity (Figure 5(b)). The activation energies observed in this study for $Li_{1.5}Al_{0.5}Hf_{1.5}(PO_4)_3$ are significantly lower than those reported for pure $LiZr_2(PO_4)_3$ (0.43 - 0.56 eV) and $LiSn_2(PO_4)_3$ (0.68 eV), suggesting a more efficient Li^+ transport in the Al-doped LHP system [66-69].

Figure 5

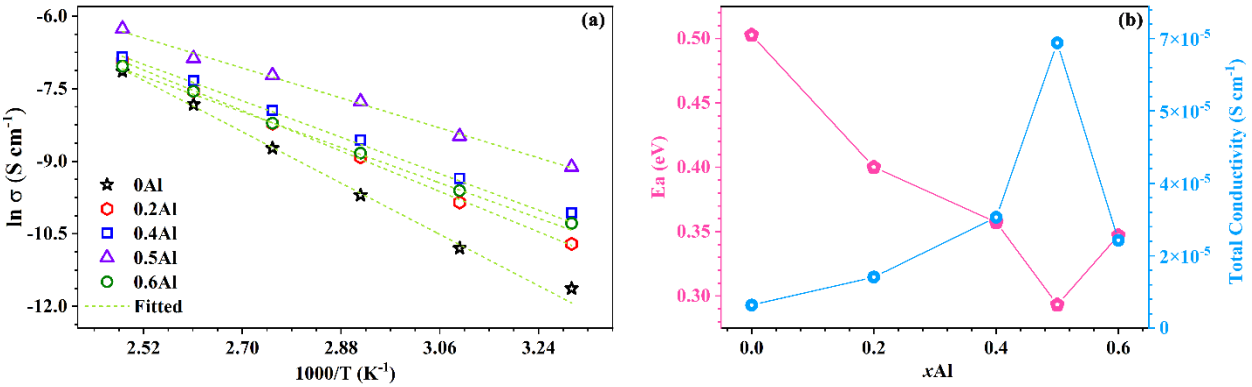

Figure 5. (a) Temperature dependence of conductivity for xAl-LHP, with dashed lines representing linear fits to the Arrhenius equation, and (b) Variation of activation energy (E_a) and total conductivity with x in $Li_{1+x}Al_xHf_{2-x}(PO_4)_3$.

Direct current (DC) polarization measurements were conducted at room temperature to evaluate the lithium-ion conductivity component of the 0.5Al-LHP sample, employing silver (Ag) blocking electrodes. As depicted in Figure 6(a), an initial rapid decay in current was observed, eventually reaching a steady state. This behavior is attributed to the blocking nature of the Ag electrodes, which impede lithium-ion movement, allowing only electronic charge carriers to contribute to the steady-state current. The lithium-ion transference number (t_{Li^+}) was calculated using the formula $t_{Li^+} = 1 - (I_e^- / I_{total})$, where I_{total} denotes the initial current, and I_e^- is the steady-state current. The calculated t_{Li^+} value of ~ 0.99 confirms the predominantly ionic nature of conduction in the 0.5Al-LHP sample.

The interfacial compatibility between the NASICON electrolyte and electrodes is crucial for the electrochemical performance of solid-state batteries (SSBs). Impedance spectroscopy measurements on the 0.5Al-LHP pellet with lithium metal electrodes, which are non-blocking for lithium ions, revealed a single depressed semicircle (Figure 6(b)). This observation confirms

lithium-ion conduction within the 0.5Al-LHP electrolyte. Galvanostatic cycling tests of lithium stripping and plating at a current density of 0.01 mA·cm^{-2} demonstrated high stability over 170 h, with a minimal increase in voltage polarization from approximately 0.11 V in the 1st cycle to ~ 0.15 V in the 173rd cycle. This slight rise in polarization is attributed to the gradual formation of a passivation layer (Figure 6(c)). This suggests robust interfacial stability between lithium metal and the as-prepared NASICON electrolyte. Additionally, critical current density (CCD) measurements performed at various current densities indicated a CCD value of 0.07 mA cm^{-2} (Figure 6(d)). In contrast, the 0.4Al and 0.6Al compositions exhibited higher initial overpotentials, which increased from 0.36 V (1st cycle) to 1.07 V (29th cycle) and from ~0.21 V (1st cycle) to ~0.24 V (29th cycle), respectively, indicating progressive interfacial degradation consistent with their lower ionic conductivities (Figs. S9–S10).

Figure 6

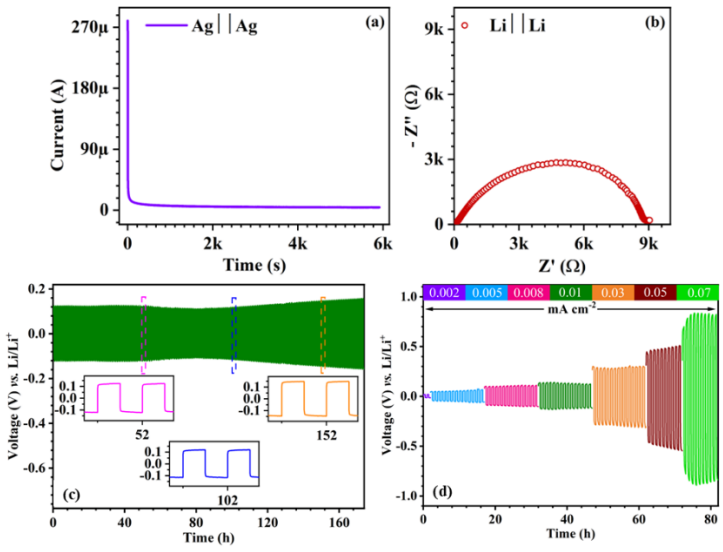

Figure 6. (a) Current vs. time response for the Ag|$Li_{1.5}Al_{0.5}Hf_{1.5}(PO_4)_3$|Ag cell under a 500 mV DC voltage. (b) Nyquist plot for the Li|$Li_{1.5}Al_{0.5}Hf_{1.5}(PO_4)_3$|Li symmetric cell at 25 °C. (c)

Galvanostatic cycling of Li stripping/plating in a symmetric cell at a current density of 0.01 mA·cm⁻². (d) Li plating/stripping behavior at varying current densities.

Linear sweep voltammetry (LSV) measurements conducted on Ag|0.5Al-LHP|Li cells revealed an electrochemical stability window of ~4.61 V (Figure 7(a). This value was determined by identifying the crossover point of two tangent lines on the LSV curve, a method commonly employed in electrochemical analysis [70]. The observed stability is attributed to the structural integrity of the NASICON framework, which effectively accommodates the substitution of hafnium with aluminum without compromising electrochemical performance.

To further assess the practical applicability of 0.5Al-LHP electrolyte, solid-state cells were assembled using $LiFePO_4$ (LFP) as the cathode and lithium metal as the anode. These cells demonstrated an initial discharge capacity of 158 mAh g^{-1}, with a retention of ~87% after 100 cycles at a rate of 0.1C (0.02 mA cm^{-2}) at room temperature (Figure 7(b-c)). Post-cycling SEM and EDS analyses revealed no signs of surface irregularities or notable chemical changes (Figure S11). Additionally, the XPS spectra (Al 2*p*, Hf 4*f*, and P 2*p*) before and after cycling showed no changes, indicating chemical stability of the ceramic electrolyte interface with lithium metal (Figure S12). Figure S13 shows the solid-state cell performance at different C-rates. Upon increasing the current, the specific capacity decreases to ~122 mAh g^{-1} (at 0.3C) and ~82 mAh g^{-1} (at 0.5C). This reduced specific capacity is due to the high resistance of the ceramic electrolyte, which becomes the rate-determining factor. The cell nearly regains its initial discharge capacity of 156 mAh g^{-1} when the current decreases back to 0.1C, demonstrating that there is no irreversible capacity loss. High cycling stability and capacity retention underscore the potential of 0.5Al-LHP as a viable electrolyte material for high-voltage SSB applications.

Figure 7

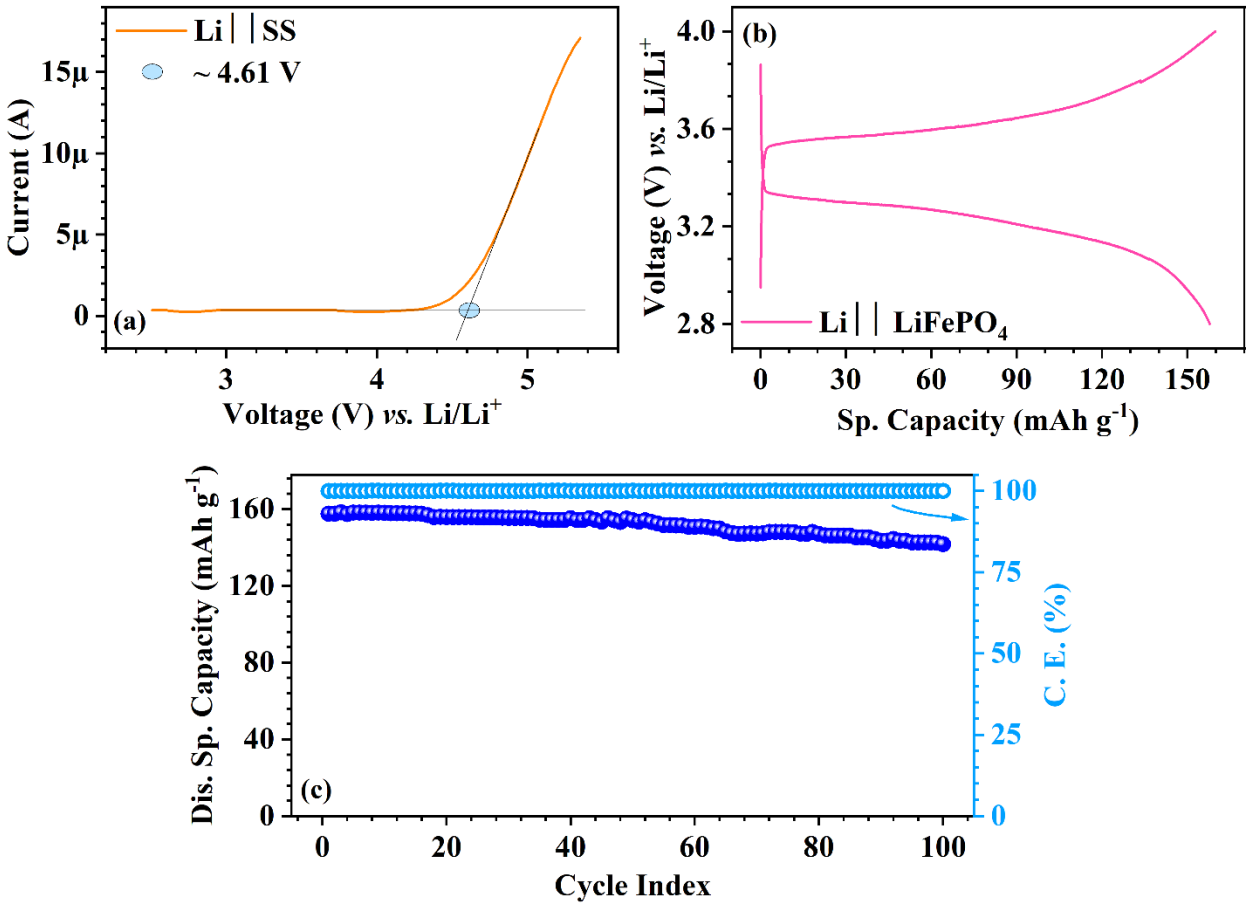

Figure 7. (a) The LSV curve of Li|$Li_{1.5}Al_{0.5}Hf_{1.5}(PO_4)_3$|SS, (b) charge-discharge curve, and (c) cycling performance of the Li| $Li_{1.5}Al_{0.5}Hf_{1.5}(PO_4)_3$|$LiFePO_4$ cell at 0.1C.

Conclusions

A rhombohedral NASICON-type solid electrolyte, $Li_{1+x}Al_xHf_{2-x}(PO_4)_3$, was synthesized using the solid-state reaction method. With increasing Al content, the lattice parameters and unit cell volume of the material decreased till x = 0.5. Among the samples analyzed, $Li_{1+x}Al_xHf_{2-x}(PO_4)_3$ with x = 0.5 exhibited the highest Li-ion conductivity ($\sigma = 7.09 \times 10^{-5}$ S^{-1} cm^{-1}) and a low activation energy of 0.29 eV. The Li-ion transference number was approximately 0.99, indicating that Li-ion conduction predominates in the material. In galvanostatic lithium plating-stripping tests, a symmetric Li|0.5Al-LHP|Li cell demonstrated stable lithium plating-stripping for over 170 h,

showing a stable interface between electrolyte/electrode. Due to the excellent stability of $Li_{1.5}Al_{0.5}Hf_{2.5}(PO_4)_3$, the solid-state Li||LFP cell showed stable cycling, maintaining high capacity (~ 87 % capacity retention) and Coulombic efficiency. These findings suggest that Al substitution in NASICON-type electrolytes enhances both ionic conductivity and anodic stability, making 0.5Al-LHP a promising candidate for next-generation solid-state batteries.

Supporting Information

Supplementary data include room temperature XRD patterns of all Al-substituted $LiHf_2(PO_4)_3$ samples, crystal structures, EDS mappings of rhombohedral samples, fitted Bode plots of their impedance spectra, and a table of their relative densities.

Author Information

Corresponding Author

Sunil Kumar - Department of Metallurgical Engineering and Materials Science, Indian Institute of Technology Indore, Simrol, 453552, India. E-mail: sunil@iiti.ac.in.

Author

Pratiksha Gami - Department of Metallurgical Engineering and Materials Science, Indian Institute of Technology Indore, Simrol, 453552, India.

Note

The authors declare no competing interests.

Acknowledgments

SK thanks the Ministry of Education for funding (Grant no. MoE-STARS/STARS-2/2023-0365). The authors thank Dr. Pradeep Kumar (IIT Mandi) for their help in XPS measurements.

References

This article references 70 other publications.

1. Kim, T.-H.; Park, J.-S.; Chang, S. K.; Choi, S.; Ryu, J. H.; Song, H.-K., The Current Move of Lithium Ion Batteries Towards the Next Phase. *Advanced Energy Materials* **2012,** *2* (7), 860-872 DOI: 10.1002/aenm.201200028.

2. Manthiram, A.; Yu, X.; Wang, S., Lithium battery chemistries enabled by solid-state electrolytes. *Nature Reviews Materials* **2017,** *2* (4) 16103, DOI: 10.1038/natrevmats.2016.103.

3. Armand, M.; Tarascon, J. M., Building better batteries. *Nature* **2008,** *451* (7179), 652-657 DOI: 10.1038/451652a.

4. Tarascon, J.-M., Is lithium the new gold? *Nature Chemistry* **2010,** *2* (6), 510-510 DOI: 10.1038/nchem.680.

5. Van der Ven, A.; Deng, Z.; Banerjee, S.; Ong, S. P., Rechargeable Alkali-Ion Battery Materials: Theory and Computation. *Chemical Reviews* **2020,** *120* (14), 6977-7019 DOI: 10.1021/acs.chemrev.9b00601.

6. Goodenough, J. B.; Park, K. S., The Li-ion rechargeable battery: a perspective. *Journal of the American Chemical Society* **2013,** *135* (4), 1167-76 DOI: 10.1021/ja3091438.

7. Dunn, B.; Kamath, H.; Tarascon, J. M., Electrical energy storage for the grid: a battery of choices. *Science* **2011,** *334* (6058), 928-35 DOI: 10.1126/science.1212741.

8. Xu, K., Electrolytes and Interphases in Li-Ion Batteries and Beyond. *Chemical Reviews* **2014,** *114* (23), 11503-11618 DOI: 10.1021/cr500003w.

9. Zhao, Y.; Bai, Y.; Li, W.; An, M.; Bai, Y.; Chen, G., Design Strategies for Polymer Electrolytes with Ether and Carbonate Groups for Solid-State Lithium Metal Batteries. *Chemistry of Materials* **2020,** *32* (16), 6811-6830 DOI: 10.1021/acs.chemmater.9b04521.

10. Yang, C.; Wu, Q.; Xie, W.; Zhang, X.; Brozena, A.; Zheng, J.; Garaga, M. N.; Ko, B. H.; Mao, Y.; He, S.; Gao, Y.; Wang, P.; Tyagi, M.; Jiao, F.; Briber, R.; Albertus, P.; Wang, C.; Greenbaum, S.; Hu, Y.-Y.; Isogai, A.; Winter, M.; Xu, K.; Qi, Y.; Hu, L., Copper-coordinated cellulose ion conductors for solid-state batteries. *Nature* **2021,** *598* (7882), 590-596 DOI: 10.1038/s41586-021-03885-6.

11. Banerjee, A.; Wang, X.; Fang, C.; Wu, E. A.; Meng, Y. S., Interfaces and Interphases in All-Solid-State Batteries with Inorganic Solid Electrolytes. *Chem Rev* **2020,** *120* (14), 6878-6933 DOI: 10.1021/acs.chemrev.0c00101.

12. Kamaya, N.; Homma, K.; Yamakawa, Y.; Hirayama, M.; Kanno, R.; Yonemura, M.; Kamiyama, T.; Kato, Y.; Hama, S.; Kawamoto, K.; Mitsui, A., A lithium superionic conductor. *Nature Materials* **2011,** *10* (9), 682-686 DOI: 10.1038/nmat3066.

13. Yang, C.; Fu, K.; Zhang, Y.; Hitz, E.; Hu, L., Protected Lithium-Metal Anodes in Batteries: From Liquid to Solid. *Advanced Materials* **2017,** *29* (36), 1701169 DOI: 10.1002/adma.201701169.

14. Hu, Y.-S., Batteries: Getting solid. *Nature Energy* **2016,** *1*, 16042 DOI: 10.1038/nenergy.2016.42.

15. Shahid, S.; Agelin-Chaab, M., A review of thermal runaway prevention and mitigation strategies for lithium-ion batteries. *Energy Conversion and Management: X* **2022,** *16*, 100310 DOI: 10.1016/j.ecmx.2022.100310.

16. Loutati, A.; Guillon, O.; Tietz, F.; Fattakhova-Rohlfing, D., NaSICON-type solid-state Li^+ ion conductors with partial polyanionic substitution of phosphate with silicate. *Open Ceramics* **2022,** *12*, 100313 DOI: 10.1016/j.oceram.2022.100313.

17. Pervez, S. A.; Cambaz, M. A.; Thangadurai, V.; Fichtner, M., Interface in Solid-State Lithium Battery: Challenges, Progress, and Outlook. *ACS Applied Materials & Interfaces* **2019,** *11* (25), 22029-22050 DOI: 10.1021/acsami.9b02675.

18. Gami, P.; Badole, M.; Vasavan, H. N.; Das, A. K.; Saxena, S.; Dagar, N.; Srihari, V.; Kumar, S., NASICON-type medium entropy $Li_{1.5}Sn_{1.0}Al_{0.5}Zr_{0.5}(PO_4)_3$ electrolyte for solid state Li metal batteries. *Journal of Power Sources* **2024,** *618*, 235214 DOI: 10.1016/j.jpowsour.2024.235214.

19. Whittingham, M. S., Lithium Batteries and Cathode Materials. *Chemical Reviews* **2004,** *104* (10), 4271-4302 DOI: 10.1021/cr020731c.

20. Chen, Z.; Kim, G.-T.; Wang, Z.; Bresser, D.; Qin, B.; Geiger, D.; Kaiser, U.; Wang, X.; Shen, Z.; Passerini, S., 4-V flexible all-solid-state lithium polymer batteries. *Nano Energy* **2019,** *64*, 103986 DOI: 10.1016/j.nanoen.2019.103986.

21. Xin, S.; You, Y.; Wang, S.; Gao, H.-C.; Yin, Y.-X.; Guo, Y.-G., Solid-State Lithium Metal Batteries Promoted by Nanotechnology: Progress and Prospects. *ACS Energy Letters* **2017,** *2* (6), 1385-1394 DOI: 10.1021/acsenergylett.7b00175.

22. Hatzell, K. B.; Chen, X. C.; Cobb, C. L.; Dasgupta, N. P.; Dixit, M. B.; Marbella, L. E.; McDowell, M. T.; Mukherjee, P. P.; Verma, A.; Viswanathan, V.; Westover, A. S.; Zeier, W. G., Challenges in Lithium Metal Anodes for Solid-State Batteries. *ACS Energy Letters* **2020,** *5* (3), 922-934 DOI: 10.1021/acsenergylett.9b02668.

23. Scrosati, B., Recent advances in lithium ion battery materials. *Electrochimica Acta* **2000,** *45*, 2461-2466 DOI: 10.1016/S0013-4686(00)00333-9.

24. Palacín, M. R., Recent advances in rechargeable battery materials: a chemist's perspective. *Chemical Society Reviews* **2009,** *38* (9), 2565-2575 DOI: 10.1039/B820555.

25. Yao, L.; Xu, S.; Tang, A.; Zhou, F.; Hou, J.; Xiao, Y.; Fu, Z., A Review of Lithium-Ion Battery State of Health Estimation and Prediction Methods. *World Electric Vehicle Journal* **2021,** *12* (3), 113 DOI: 10.3390/wevj12030113

26. Jian, Z.; Hu, Y.-S.; Ji, X.; Chen, W., NASICON-Structured Materials for Energy Storage. *Advanced Materials* **2017,** *29* (20), 1601925 DOI: 10.1002/adma.201601925.

27. Das, A. K.; Badole, M.; Vasavan, H. N.; Saxena, S.; Gami, P.; Kumar, S., Highly conductive ceramic-in-polymer composite electrolyte enabling superior electrochemical performance for all-solid-state lithium batteries. *Ceramics International* **2023,** *49* (18), 29719-29728 DOI: 10.1016/j.ceramint.2023.06.214.

28. Gami, P.; Badole, M.; Vasavan, H. N.; Das, A. K.; Saxena, S.; Kumar, S., Y-Doped $LiZr_2(PO_4)_3$ in a PVDF-HFP Composite Electrolyte for Solid-State Li-Metal Batteries. *ACS Applied Engineering Materials* **2024,** *2* (5), 1278-1287 DOI: 10.1021/acsaenm.4c00076.

29. Radjendirane, A. C.; Maurya, D. K.; Ren, J.; Hou, H.; Algadi, H.; Xu, B. B.; Guo, Z.; Angaiah, S., Overview of Inorganic Electrolytes for All-Solid-State Sodium Batteries. *Langmuir* **2024,** *40* (32), 16690-16712 DOI: 10.1021/acs.langmuir.4c01845.

30. Gami, P.; Badole, M.; Das, A. K.; Vasavan, H. N.; Saxena, S.; Dagar, N.; Kumar, S., PVP incorporation effects on the structural, thermal, electrical, and mechanical properties of PVDF-HFP/PVP blend. *Journal of Polymer Research* **2025,** *32* (3), 94 DOI: 10.1007/s10965-025-04321-3.

31. Zheng, F.; Kotobuki, M.; Song, S.; Lai, M.; Lu, L., Review on solid electrolytes for all-solid-state lithium-ion batteries. *Journal of Power Sources* **2018,** *389*, 198-213 DOI: 10.1016/j.jpowsour.2018.04.022.

32. Sun, C.; Liu, J.; Gong, Y.; Wilkinson, D. P.; Zhang, J., Recent advances in all-solid-state rechargeable lithium batteries. *Nano Energy* **2017,** *33*, 363-386 DOI: 10.1016/j.nanoen.2017.01.028.

33. Tao, B.; Ren, C.; Li, H.; Liu, B.; Jia, X.; Dong, X.; Zhang, S.; Chang, H., Thio-/LISICON and LGPS-Type Solid Electrolytes for All-Solid-State Lithium-Ion Batteries. *Advanced Functional Materials* **2022,** *32* (34), 2203551 DOI: 10.1002/adfm.202203551.

34. Li, S.; Yang, Z.; Wang, S.-B.; Ye, M.; He, H.; Zhang, X.; Nan, C.-W.; Wang, S., Sulfide-based composite solid electrolyte films for all-solid-state batteries. *Communications Materials* **2024,** *5* (1), 44 DOI: 10.1038/s43246-024-00482-8.

35. Murugan, R.; Thangadurai, V.; Weppner, W., Fast Lithium Ion Conduction in Garnet-Type $Li_7La_3Zr_2O_{12}$. *Angewandte Chemie International Edition* **2007,** *46* (41), 7778-7781 DOI: 10.1002/anie.200701144.

36. Thangadurai, V.; Weppner, W., $Li_6ALa_2Ta_2O_{12}$ (A = Sr, Ba): Novel Garnet-Like Oxides for Fast Lithium Ion Conduction. *Advanced Functional Materials* **2005,** *15* (1), 107-112 DOI: 10.1002/adfm.200400044.

37. Feng, Y.; Yang, L.; Yan, Z.; Zuo, D.; Zhu, Z.; Zeng, L.; Zhu, Y.; Wan, J., Discovery of high entropy garnet solid-state electrolytes via ultrafast synthesis. *Energy Storage Materials* **2023,** *63*, 103053 DOI: 10.1016/j.ensm.2023.103053.

38. Das, A. K.; Badole, M.; Vasavan, H. N.; Saxena, S.; Gami, P.; Dagar, N.; Kumar, S., Integrated cathode-electrolyte ($Li_{6.55}La_3Zr_{1.55}Ta_{0.45}O_{12}$/PEO-LiTFSI) architecture driven excellent performance of solid-state lithium metal batteries. *Journal of Energy Storage* **2024,** *94*, 112452 DOI: 10.1016/j.est.2024.112452.

39. Singh, K.; Chakraborty, A.; Thirupathi, R.; Omar, S., Recent advances in NASICON-type oxide electrolytes for solid-state sodium-ion rechargeable batteries. *Ionics* **2022,** *28* (12), 5289-5319 DOI: 10.1007/s11581-022-04765-3.

40. Yamamoto, H.; Tabuchi, M.; Takeuchi, T.; Kageyama, H.; Nakamura, O., Ionic conductivity enhancement in $LiGe_2(PO_4)_3$ solid electrolyte. *Journal of Power Sources* **1997,** *68* (2), 397-401 DOI: 10.1016/S0378-7753(97)02541-X.

41. Li, Y.; Liu, M.; Liu, K.; Wang, C.-A., High Li+ conduction in NASICON-type Li1+xYxZr2−x(PO4)3 at room temperature. *Journal of Power Sources* **2013,** *240*, 50-53 DOI: 10.1016/j.jpowsour.2013.03.175.

42. Safanama, D.; Sharma, N.; Rao, R. P.; Brand, H. E. A.; Adams, S., Structural evolution of NASICON-type $Li_{1+x}Al_xGe_{2-x}(PO_4)_3$ using in situ synchrotron X-ray powder diffraction. *Journal of Materials Chemistry A* **2016,** *4* (20), 7718-7726 DOI: 10.1039/C6TA00402D.

43. Stenina, I.; Novikova, S.; Voropaeva, D.; Yaroslavtsev, A., Solid Electrolytes Based on NASICON-Structured Phosphates for Lithium Metal Batteries. *Batteries* **2023,** *9* (8) 407, DOI: 10.3390/batteries9080407.

44. Ortiz, G. F.; López, M. C.; Lavela, P.; Vidal-Abarca, C.; Tirado, J. L., Improved lithium-ion transport in NASICON-type lithium titanium phosphate by calcium and iron doping. *Solid State Ionics* **2014,** *262*, 573-577 DOI: 10.1016/j.ssi.2013.09.012.

45. Gami, P.; Das, A. K.; Badole, M.; Vasavan, H. N.; Saxena, S.; Dagar, N.; Deswal, S.; Kumar, P.; Dwivedi, A.; Poswal, H. K.; Kumar, S., Fostering Li-ion conduction in Zr-Sn-Al-based mid-entropy NASICON electrolyte. *Ceramics International* **2024,** *50* (22, Part C), 47612-47619 DOI: 10.1016/j.ceramint.2024.09.107.

46. Das, A. K.; Badole, M.; Vasavan, H. N.; Saxena, S.; Gami, P.; Deswal, S.; Kumar, P.; Kumar, S., Enhancing room temperature performance of solid-state lithium cell via a facile solid electrolyte-cathode interface design. *Materials Today Sustainability* **2024,** *26*, 100758 DOI: 10.1016/j.mtsust.2024.100758.

47. Das, A. K.; Gami, P.; Vasavan, H. N.; Saxena, S.; Dagar, N.; Deswal, S.; Kumar, P.; Kumar, S., Advancing High-Energy Solid-State Batteries with High-Entropy NASICON-type Solid Electrolytes. *ACS Applied Energy Materials* **2024,** *7* (19), 8301-8307 DOI: 10.1021/acsaem.4c02011.

48. Losilla, E. R.; Aranda, M. A. G.; Martínez-Lara, M.; Bruque, S., Reversible Triclinic-Rhombohedral Phase Transition in $LiHf_2(PO_4)_3$: Crystal Structures from Neutron Powder Diffraction. *Chemistry of Materials* **1997,** *9* (7), 1678-1685 DOI: 10.1021/cm970078n.

49. Martínez-Juárez, A.; Amarilla, J. M.; Iglesias, J. E.; Rojo, J. M., Ionic conductivity of $LiHf_2(PO_4)_3$ with NASICON-type structure and its possible application as electrolyte in lithium batteries. *Journal of the Brazilian Chemical Society* **1997,** *8 (3)*, 261-264 DOI: 10.1590/S0103-50531997000300014.

50. Aono, H.; Sugimoto, E.; Sadaoka, Y.; Imanaka, N.; Adachi, G.-y., Electrical properties and crystal structure of solid electrolyte based on lithium hafnium phosphate $LiHf_2(PO_4)_3$. *Solid State Ionics* **1993,** *62* (3), 309-316 DOI: 10.1016/0167-2738(93)90387-I.

51. Zangina, T.; Hassan, J.; Azis, R. a. S.; Matori, K. A.; See, A.; Alibe, I. M.; Umar, S., Structural, electrical conductivity and dielectric relaxation behavior of $LiHf_2(PO_4)_3$ ceramic powders. *Journal of the Australian Ceramic Society* **2018,** *54* (2), 307-316 DOI: 10.1007/s41779-017-0155-2.

52. Li, Q.-H.; Xu, C.; Huang, B.; Yin, X., Sr^{2+}-doped rhombohedral $LiHf_2(PO_4)_3$ solid electrolyte for all-solid-state Li-metal battery. *Rare Metals* **2020,** *39* (9), 1092-1098 DOI: 10.1007/s12598-020-01441-1.

53. Zangina, T.; Hassan, J.; Azis, R. a. S.; Matori, K. A.; Khoon, T. F.; Musa, M. A., Analysis of thermal and electrical conductivity properties of Al substitution $LiHf_2(PO_4)_3$ chemical solid electrolyte. *SN Applied Sciences* **2019,** *1* (8), 863 DOI: 10.1007/s42452-019-0901-x.

54. Chang, C.-M.; Hong, S.-H.; Park, H.-M., Spark plasma sintering of Al substituted $LiHf_2(PO_4)_3$ solid electrolytes. *Solid State Ionics* **2005,** *176* (35), 2583-2587 DOI: 10.1016/j.ssi.2005.07.010.

55. Coelho, A. A., TOPAS and TOPAS-Academic: an optimization program integrating computer algebra and crystallographic objects written in C++. *Journal of Applied Crystallography* **2018,** *51* (1), 210-218 DOI: 10.1107/S1600576718000183.

56. Ragoisha, G.; Bondarenko, A., EIS spectrum analyser. **2016**.

57. C.P, S.; B.V, S. K.; Naik, A., Comparative Study of Hydrothermally Synthesized $AlPO_4$-5, Activated Carbon, and the Combination of Activated Carbon and $AlPO_4$-5 Filters in the Treatment of Wastewater and Industrial Effluent. *Water Conservation Science and Engineering* **2016,** *1* (3), 177-195 DOI: 10.1007/s41101-016-0012-0.

58. Weiss, M.; Weber, D. A.; Senyshyn, A.; Janek, J.; Zeier, W. G., Correlating Transport and Structural Properties in $Li_{1+x}Al_xGe_{2-x}(PO_4)_3$ (LAGP) Prepared from Aqueous Solution. *ACS Applied Materials & Interfaces* **2018,** *10* (13), 10935-10944 DOI: 10.1021/acsami.8b00842.

59. Cretin, M.; Fabry, P., Comparative study of lithium ion conductors in the system $Li_{1+x}Al_xA_{2-x}^{IV}(PO_4)_3$ with A^{IV}=Ti or Ge and $0 \leq x \leq 0{\cdot}7$ for use as Li^+ sensitive membranes. *Journal*

of the European Ceramic Society **1999,** *19* (16), 2931-2940 DOI: 10.1016/S0955-2219(99)00055-2.

60. Giarola, M.; Sanson, A.; Tietz, F.; Pristat, S.; Dashjav, E.; Rettenwander, D.; Redhammer, G. J.; Mariotto, G., Structure and Vibrational Dynamics of NASICON-Type $LiTi_2(PO_4)_3$. *The Journal of Physical Chemistry C* **2017,** *121* (7), 3697-3706 DOI: 10.1021/acs.jpcc.6b11067.

61. Redhammer, G. J.; Rettenwander, D.; Pristat, S.; Dashjav, E.; Kumar, C. M. N.; Topa, D.; Tietz, F., A single crystal X-ray and powder neutron diffraction study on NASICON-type $Li_{1+x}Al_xTi_{2-x}(PO_4)_3$ ($0 \leq x \leq 0.5$) crystals: Implications on ionic conductivity. *Solid State Sciences* **2016,** *60*, 99-107 DOI: 10.1016/j.solidstatesciences.2016.08.011.

62. Akkinepally, B.; Ithereddy, N. R.; Shim, J., Lithium Ion Transport in Al-Doped $LiZr_2(PO_4)_3$ Solid Electrolyte for Li-Air Batteries: Experimental and Molecular Dynamics Study with a Touch of Machine Learning. *ECS Meeting Abstracts* **2021,** *MA2021-02* (1), 73 DOI: 10.1149/MA2021-02173mtgabs.

63. Luo, Y.; Jiang, X.; Yu, Y.; Liu, L.; Lin, X.; Wang, Z.; Han, L.; Luo, Z.; Lu, A., Enhancement of electrical properties of $LiTi_2(PO_4)_3$ ceramics via trivalent cation doping and microstructure regulation strategies. *Solid State Ionics* **2023,** *390*, 116111 DOI: 10.1016/j.ssi.2022.116111.

64. Francisco, B. E.; Stoldt, C. R.; M'Peko, J.-C., Energetics of Ion Transport in NASICON-Type Electrolytes. *The Journal of Physical Chemistry C* **2015,** *119* (29), 16432-16442 DOI: 10.1021/acs.jpcc.5b03286.

65. Francisco, B. E.; Stoldt, C. R.; M'Peko, J.-C., Lithium-Ion Trapping from Local Structural Distortions in Sodium Super Ionic Conductor (NASICON) Electrolytes. *Chemistry of Materials* **2014,** *26* (16), 4741-4749 DOI: 10.1021/cm5013872.

66. Kumar, S.; Balaya, P., Improved ionic conductivity in NASICON-type Sr^{2+} doped $LiZr_2(PO_4)_3$. *Solid State Ionics* **2016,** *296*, 1-6 DOI: 10.1016/j.ssi.2016.08.012.

67. Ramar, V.; Kumar, S.; Sivakkumar, S. R.; Balaya, P., NASICON-type La^{3+} substituted $LiZr_2(PO_4)_3$ with improved ionic conductivity as solid electrolyte. *Electrochimica Acta* **2018,** *271*, 120-126 DOI: 10.1016/j.electacta.2018.03.115.

68. Ahmed, S. A.; Pareek, T.; Dwivedi, S.; Badole, M.; Kumar, S., $LiSn_2(PO_4)_3$-based polymer-in-ceramic composite electrolyte with high ionic conductivity for all-solid-state lithium batteries. *Journal of Solid State Electrochemistry* **2020,** *24* (10), 2407-2417 DOI: 10.1007/s10008-020-04783-z.

69. Zhang, Y.; Chen, K.; Shen, Y.; Lin, Y.; Nan, C.-W., Enhanced lithium-ion conductivity in a $LiZr_2(PO_4)_3$ solid electrolyte by Al doping. *Ceramics International* **2017,** *43*, S598-S602 DOI: 10.1016/j.ceramint.2017.05.198.

70. Zhang, Q.; Zhou, Q.; Lu, Y.; Shao, Y.; Qi, Y.; Qi, X.; Zhong, G.; Yang, Y.; Chen, L.; Hu, Y.-S., Modification of NASICON Electrolyte and Its Application in Real Na-Ion Cells. *Engineering* **2022,** *8*, 170-180 DOI: 10.1016/j.eng.2021.04.028.

[Supplementary Material]

Tuning Ionic Conductivity and Structural Stability of $LiHf_2(PO4)_3$ Solid Electrolytes through Al Substitution

Pratiksha Gami and Sunil Kumar*

Department of Metallurgical Engineering and Materials Science, Indian Institute of Technology Indore, Simrol, 453552, India.

*Corresponding author, E-mail: sunil@iiti.ac.in

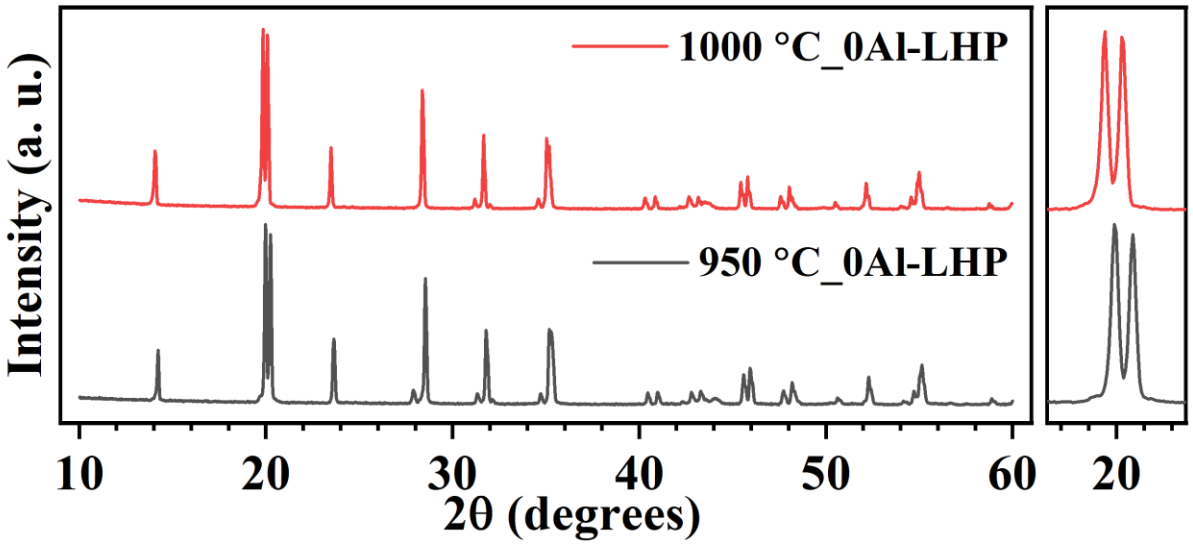

Figure S1 Room temperature powder XRD patterns of 0Al-LHP samples sintered at different temperatures.

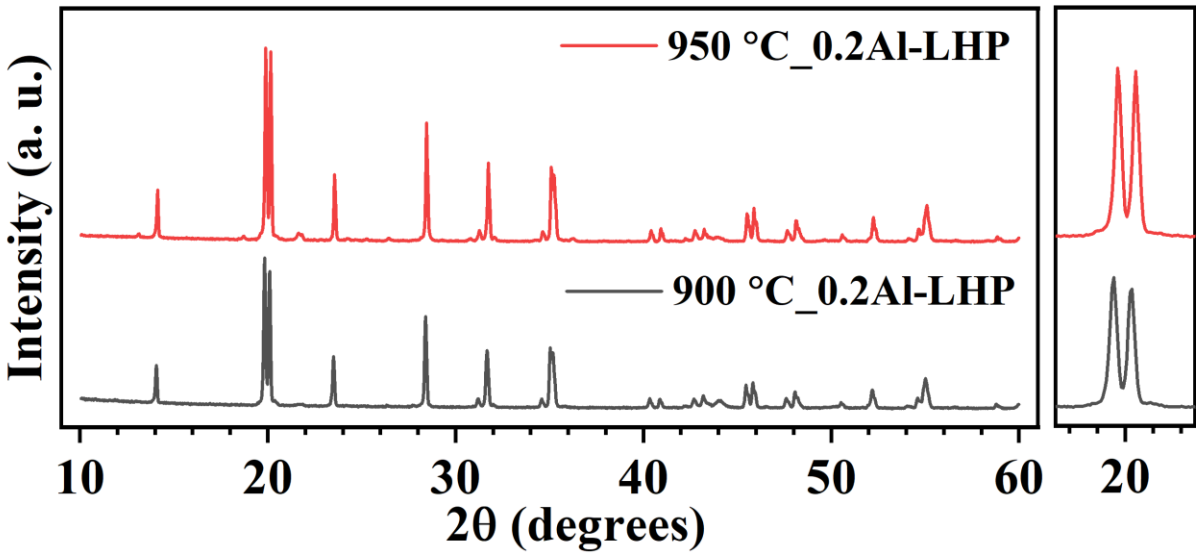

Figure S2 Room temperature powder XRD patterns of 0.2Al-LHP samples sintered at different temperatures.

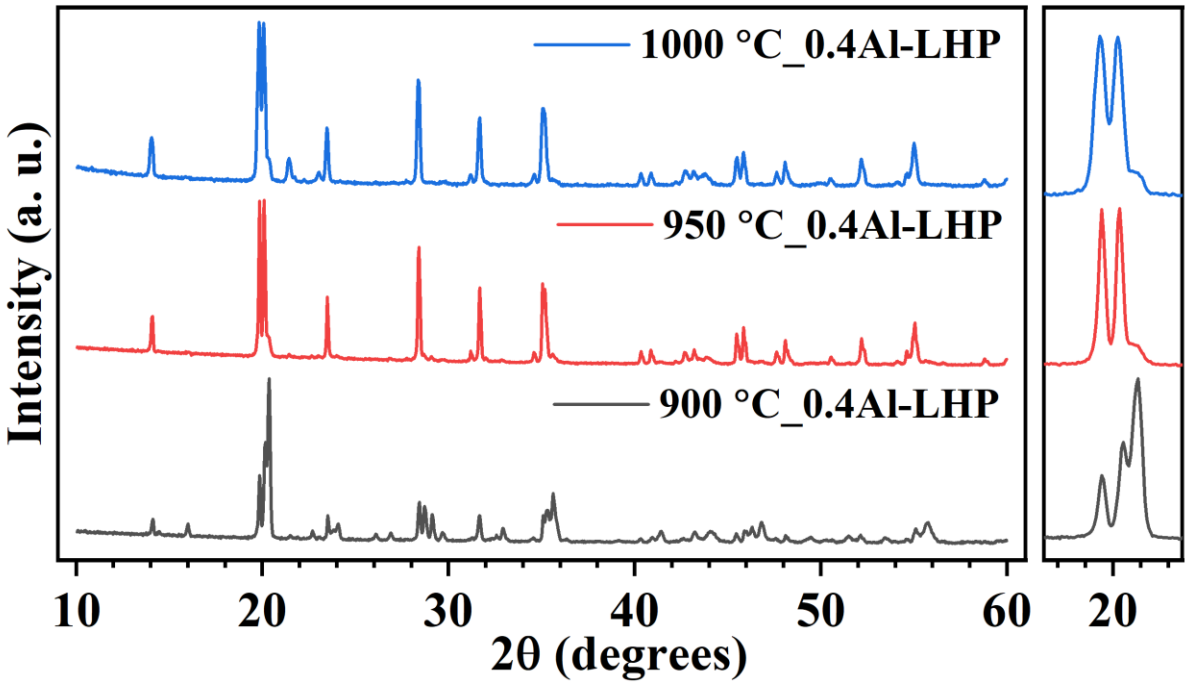

Figure S3 Room temperature powder XRD patterns of 0.4Al-LHP samples sintered at different temperatures.

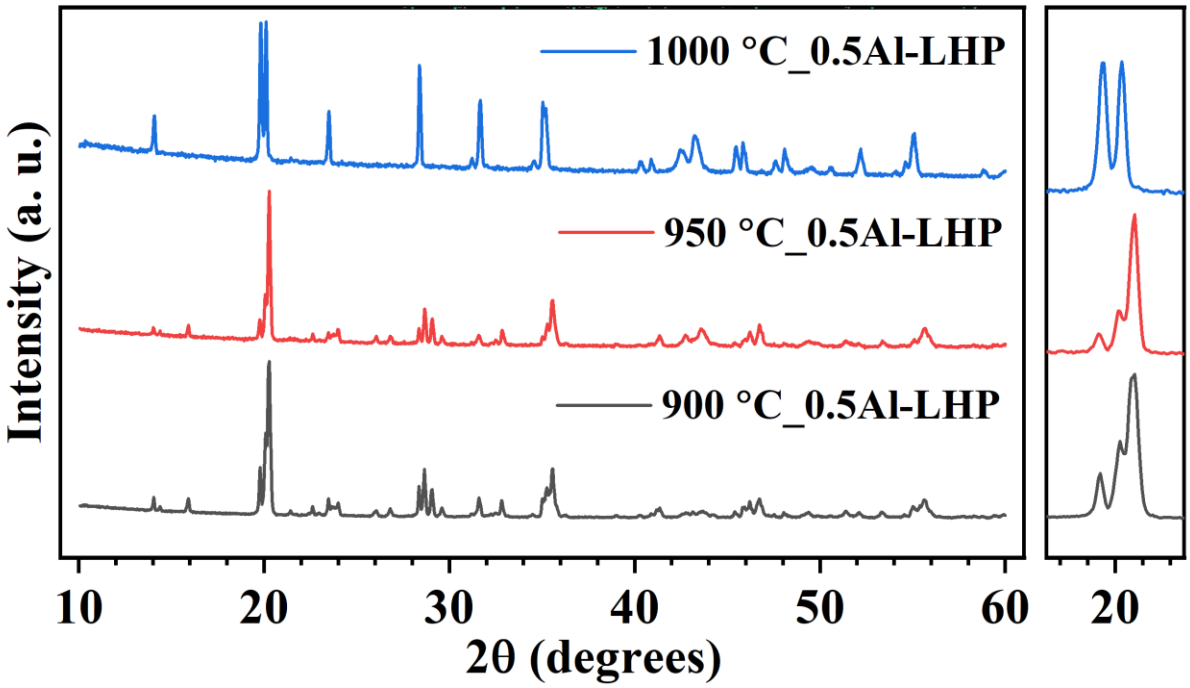

Figure S4 Room temperature powder XRD patterns of 0.5Al-LHP samples sintered at different temperatures.

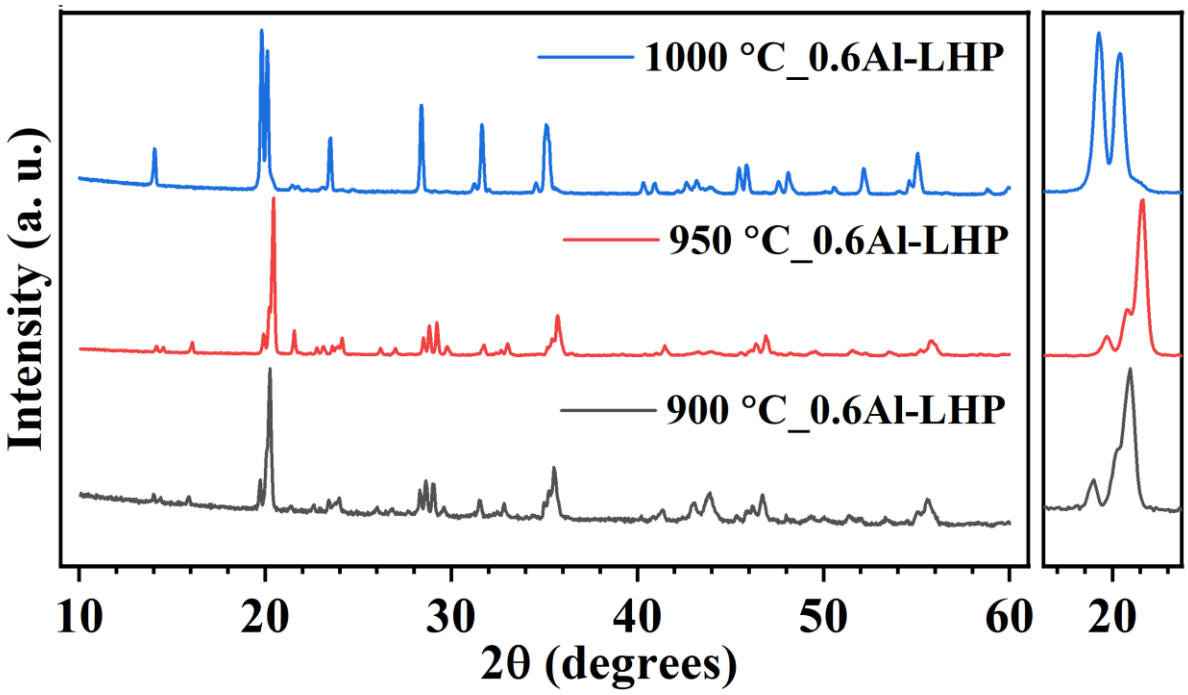

Figure S5 Room temperature powder XRD patterns of 0.6Al-LHP samples sintered at different temperatures.

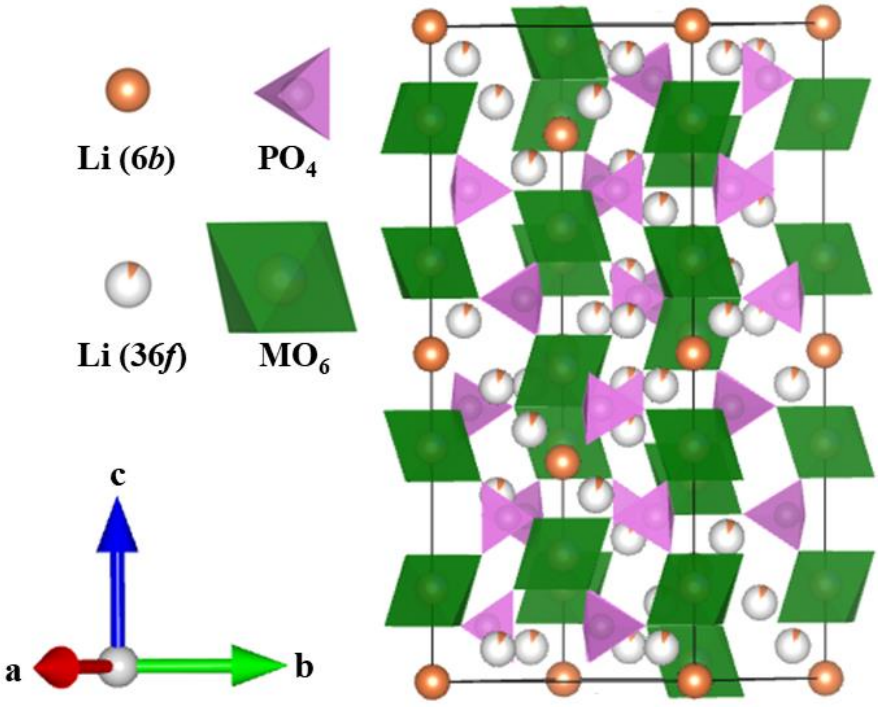

Figure S6 Crystal structure of Al-doped $Li_{1+x}Al_xHf_{2-x}(PO_4)_3$, here in MO_6 M is Al/Hf.

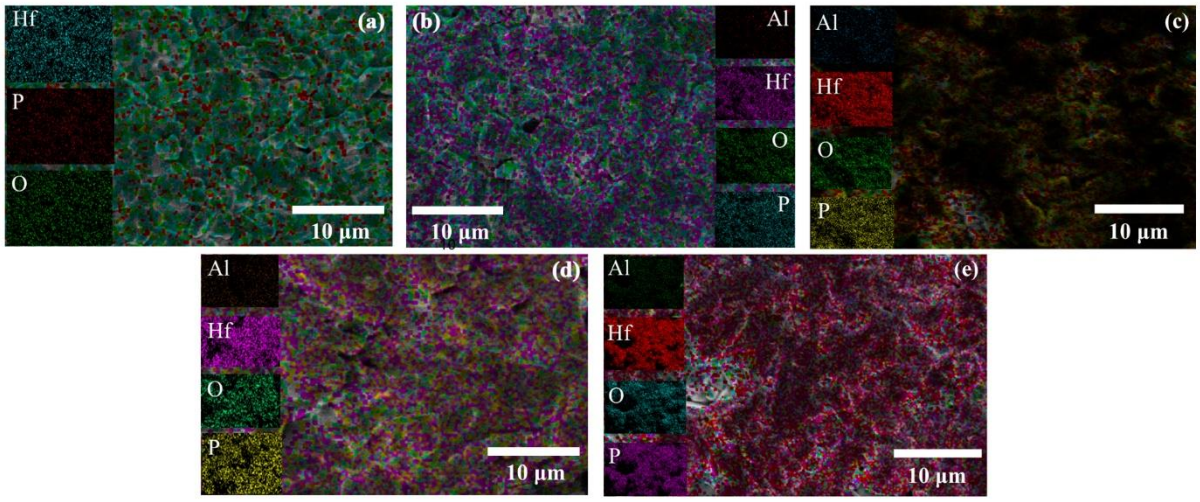

Figure S7 EDS mappings of various elements of (a) 0Al-LHP, (b) 0.2Al-LHP, (c) 0.4Al-LHP, (d) 0.5Al-LHP, and (e) 0.6Al-LHP pellet.

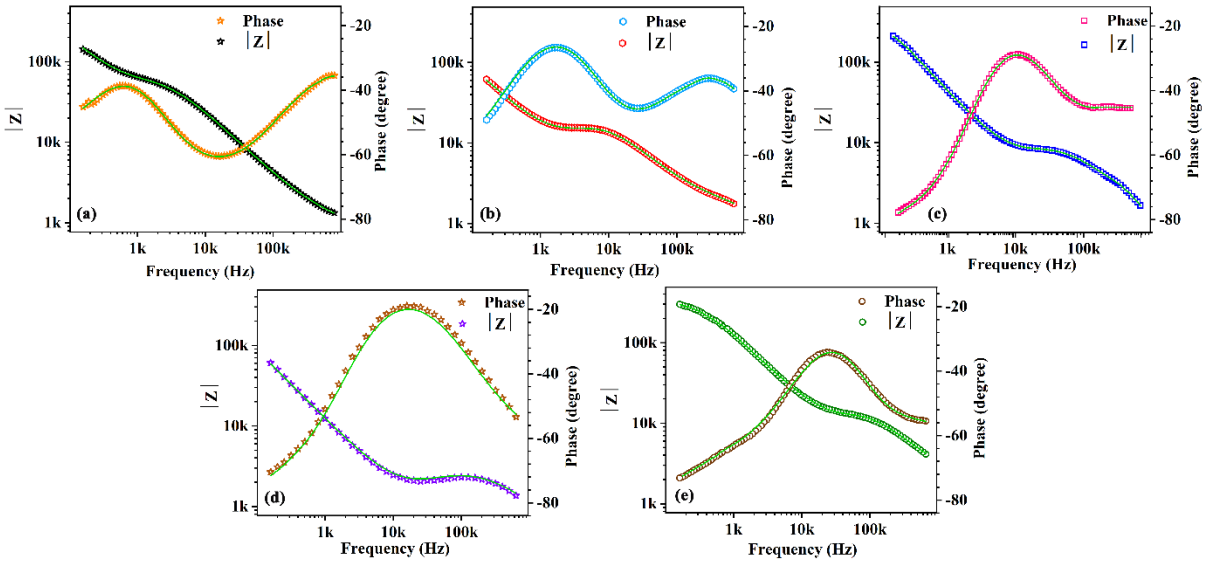

Figure S8 Fitted Bode plots of room temperature impedance data of (a) 0Al-LHP, (b) 0.2Al-LHP, (c) 0.4Al-LHP, (d) 0.5Al-LHP, and (e) 0.6Al-LHP pellet.

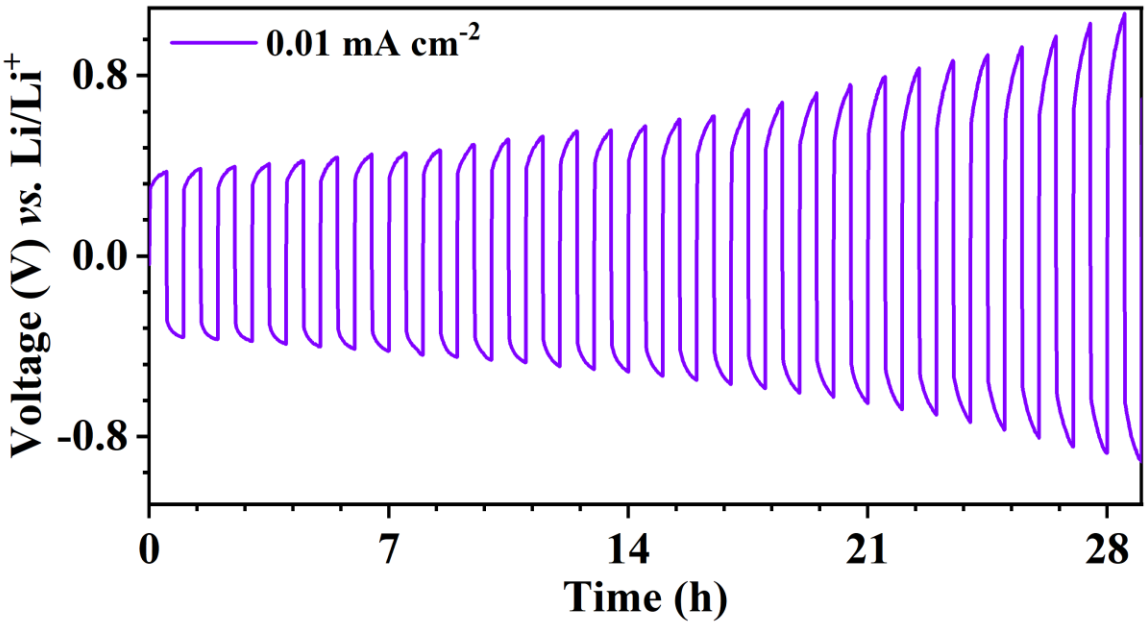

Figure S9 Galvanostatic cycling of Li stripping/plating in a symmetric $Li|Li_{1.4}Al_{0.4}Hf_{1.6}(PO_4)_3|Li$ *cell.*

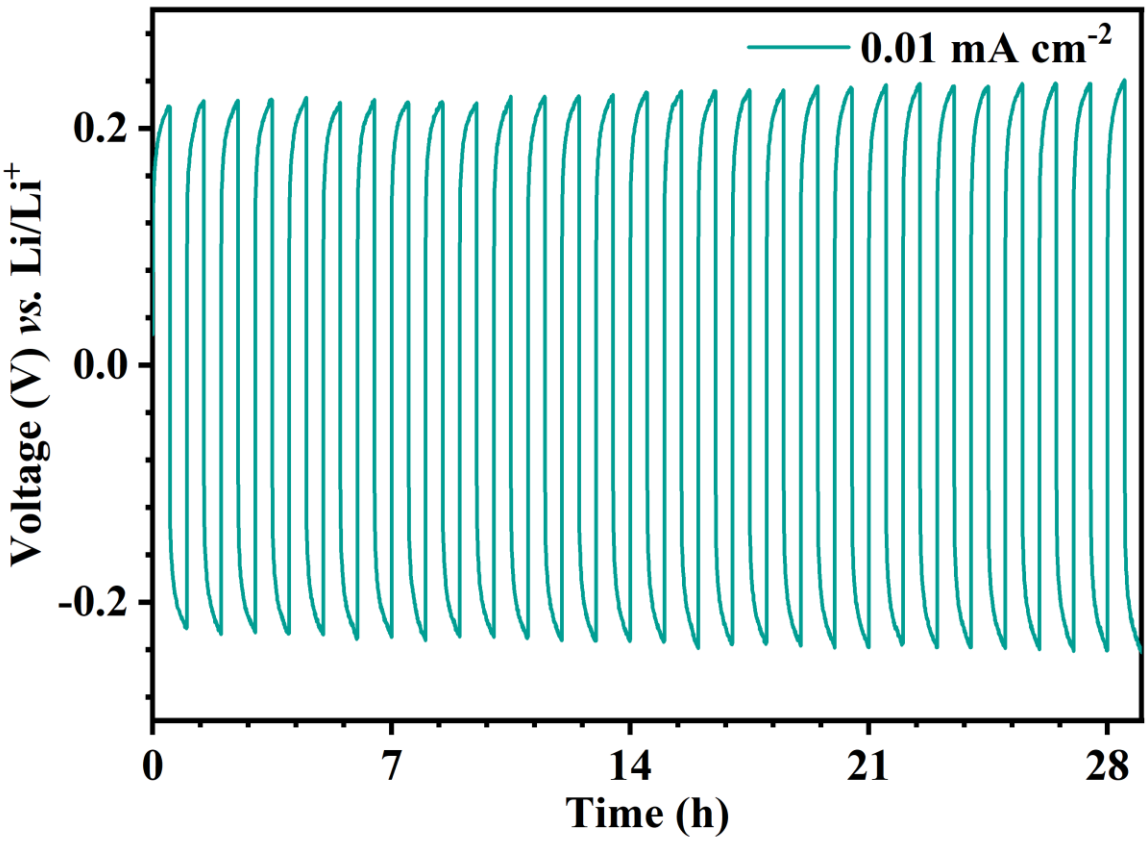

Figure S10 Galvanostatic cycling of Li stripping/plating in a symmetric $Li|Li_{1.6}Al_{0.6}Hf_{1.4}(PO_4)_3|Li$ *cell.*

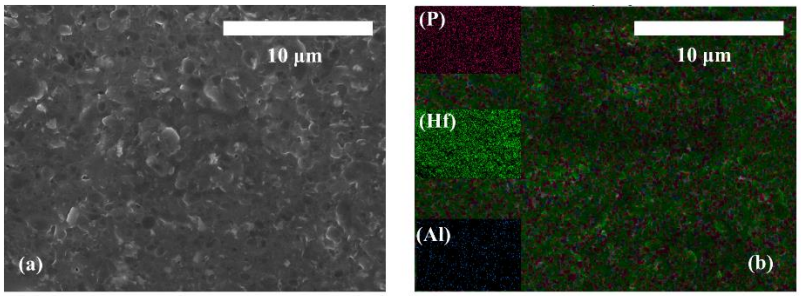

Figure S11 (a) SEM image and (b) EDS mappings (Al, Hf, and P) of cycled electrolyte pellet 0.5Al-LHP.

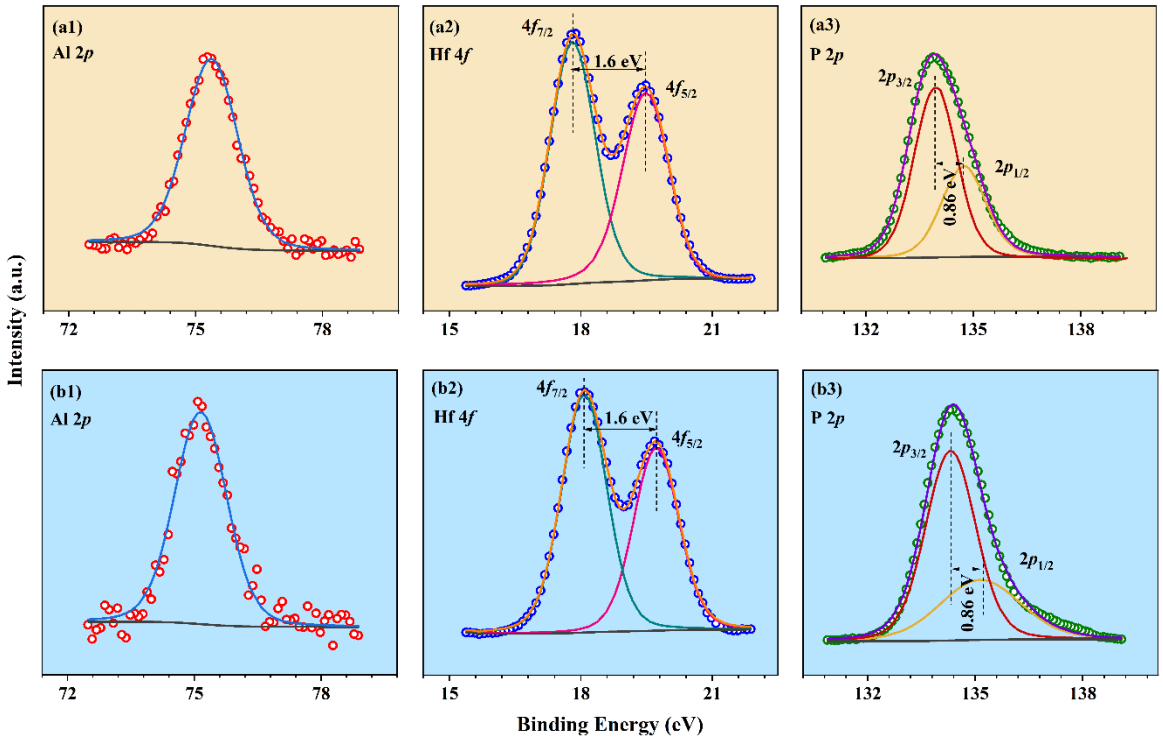

Figure S12 Fitted XPS spectra of fresh (a1-a3) and cycled (b1-b3) 0.5Al-LHP: (a1, b1) Al 2p, (a2, b2) Hf 4f, and (a3, b3) P 2p regions.

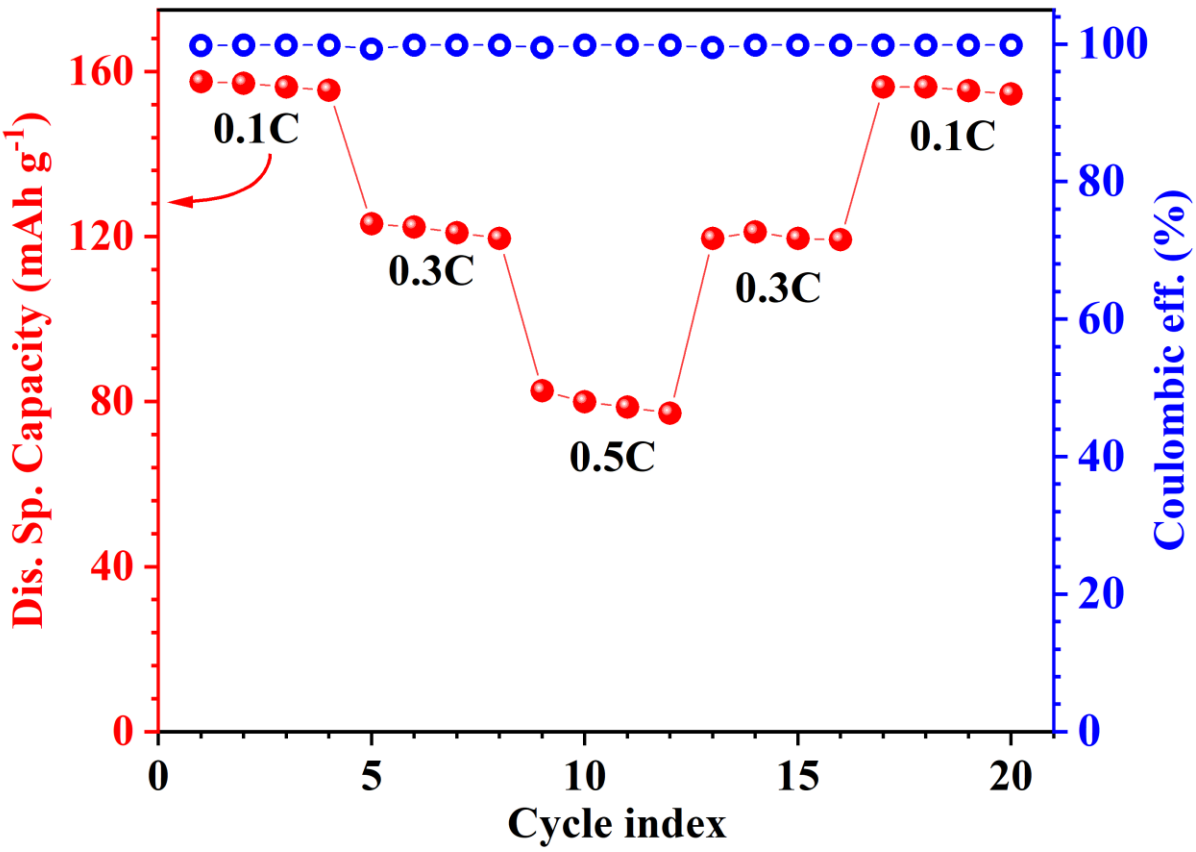

Figure S13 Rate performance of Li|$Li_{1.5}Al_{0.5}Hf_{1.5}(PO_4)_3$|$LiFePO_4$ cell.

Table S1: Relative density of various $Li_{1+x}Al_xHf_{2-x}(PO_4)_3$ pellets at different x.

x (Al content)	**Relative density (%)**
0	72 ± 0.01
0.2	78 ± 0.008
0.4	80 ± 0.005
0.5	86 ± 0.01
0.6	83 ± 0.008